The Effect of Lamellar Morphology on Tensile and High-Cycle Fatigue Behavior of Orthorhombic Ti-22Al-27Nb Alloy

MASUO HAGIWARA, AYA ARAOKA, SEUNG JIN YANG, SATOSHI EMURA, and SOO WOO NAM

The room-temperature tensile and high-cycle fatigue (HCF) behavior of orthorhombic Ti-22Al-27Nb alloy with varying lamellar morphology was investigated. Varying lamellar morphology was produced by changing the cooling rate after annealing in the single B2 phase region. A slower cooling rate of 0.003 K/s, for example, resulted in several large packets or colonies of similarly aligned O-phase lamellae and a nearly continuous massive α_2 phase at the prior B2 grain boundaries, while a faster cooling rate of 0.1 K/s led to the refinement of colony sizes and the O-phase lamellae. The interface of O-phase lamellae and B2 phases was semicoherent. Water quenching produced a very fine tweed-like microstructure with a thin continuous O phase at the prior B2 grain boundaries. The 0.2 pct yield stress, tensile strength, and HCF strength increased with increasing cooling rate. For example, the tensile strength and HCF strength at 10^7 cycles of 0.003 and 0.1 K/s-cooled were 774 and 450 MPa, and 945 and 620 MPa, respectively. Since the fatigue ratio, which is the ratio of HCF strength at 10^7 cycles to tensile strength, did not show a constant value, but instead increased with increasing cooling rate, part of the fatigue improvement was the result of improved resistance to fatigue associated with the microstructural refinement of the lamellar morphology. Fatigue failure occurred by the subsurface initiation, and every initiation site was found to contain a flat facet. Concurrent observation of the fatigue initiation facet and the underlying microstructure revealed that the fatigue crack initiated in a shear mode across the colony, irrespective of colony size, indicating that the size of the initiation facet corresponded to that of the colony. Therefore, the colony size is likely a major controlling factor in determining the degree of fatigue improvement due to the microstructural refinement of lamellar morphology. For the water-quenched specimens, fatigue crack initiation appeared to be associated with shear cracking along the boundary between the continuous grain boundary O phase and the adjacent prior B2 grain.

I. INTRODUCTION

IN the previous 2 decades, considerable efforts have been made to develop $Ti_3Al(\alpha_2)$-based and $TiAl(\gamma)$-based titanium intermetallic alloys for elevated temperature applications. However, their application is still limited by the low ductility and lack of resistance to fracture of these alloys at low temperatures.[1,2]

Recently, a new class of titanium intermetallic alloys, based on the Ti_2AlNb phase, have become the focus of attention as potential materials for aircraft engine applications due to their higher specific strength and fracture toughness than α_2-based and γ-based alloys.[3–15] These alloys are often called orthorhombic alloys because of the ordered orthorhombic structure of the Ti_2AlNb phase. One typical orthorhombic alloy is the Ti-22 at. pct Al-27at. pct Nb alloy,[3,4] which consists mainly of the Ti_2AlNb phase (O phase) and ordered B2 phase.[5] A wide range of microstructures and hence a variety of properties can be developed in a Ti-22Al-27Nb alloy through control of processing and heat treatments. For example, O-phase lamellae separated by thin B2-phase films are formed by cooling from the single B2 region, and therefore, this type of microstructure is often called a lamellar microstructure. Similar to conventional α-β type titanium alloys such as Ti-6Al-4V and Ti-6Al-2Sn-4Zr-2Mo alloys, the morphology of lamellar microstructure, *i.e.*, lamellar morphology, can be arranged in packets or colonies of similarly aligned O-phase lamellae or in a basketweave morphology depending on the cooling rate. The equiaxed O-phase microstructure can be obtained by applying a major deformation in the (O + B2) two-phase region and subsequent annealing in the same (O + B2) two-phase region.[8] During subsequent annealing, the heavily deformed O phase becomes equiaxed or spherical in shape due to recrystallization. Studies of the relationship between mechanical properties and microstructures in a Ti-22Al-27Nb alloy have revealed that, among these two typical microstructures, a lamellar microstructure has the best high-temperature properties, especially with respect to creep resistance.[3,5] Therefore, the control of processing and heat treatment needs to be carried out in order to give the Ti-22Al-27Nb alloy a lamellar microstructure.

To ensure the material's reliability, Ti-22Al-27Nb alloy should also have a very good high-cycle fatigue (HCF) property at room temperature. However, so far, there are little data available on the relationship among tensile strength, HCF strength, and lamellar morphology. The purpose of the present study therefore was to investigate the effect of lamellar morphology on tensile and HCF behavior of Ti-22Al-27Nb alloy.

MASUO HAGIWARA and SATOSHI EMURA, Senior Researchers, and AYA ARAOKA, Researcher, are with the National Institute for Materials Science, Tsukuba, Ibaraki 305-0047, Japan. Contact e-mail: hagiwara.masuo@nims.go.jp SEUNG JIN YANG, Graduate Student, and SOO WOO NAM, Professor, are with the Department of Materials Science and Engineering, Korea Advanced Institute of Science and Technology, Yuseong-gu, Daejeon, Republic of Korea.

Manuscript submitted June 2, 2003.

II. EXPERIMENTAL PROCEDURE

A Ti-22Al-27Nb alloy ingot with a diameter of about 50 mm was prepared by plasma arc melting under Ar gas atmosphere. Melting was performed 3 times to ensure homogeneity. Chemical analysis of the ingot showed Ti-22.0 at. pct Al-26.8 at. pct Nb and oxygen content of 640 ppm. The alloy ingot was first hot rolled at 1423 K in the B2-phase region into 12-mm square bars. Hot rolling was performed using 16 passes, with the rolled bars reheated every 2 passes. These rolled bars were annealed at 1423 K for 3.6 ks and then cooled to produce a lamellar microstructure. The lamellar morphology was varied by changing the cooling rate. Four different cooling rates were applied, *i.e.*, 0.003 K/s (very slow furnace cooling), 0.03 K/s (slow furnace cooling), 0.1 K/s (fast furnace cooling), and water quenching (about 130 K/s[16]). The controlled cooling in the furnace was maintained until the temperature reached 873 K, after which air cooling was applied. These cooled bars were finally held at 1123 K for 118.8 ks in the (B2 + O) two-phase region[5] to stabilize the microstructure. These heat-treatment conditions are listed in Table I.

Room-temperature tensile tests were performed in air with specimens 3.5 mm in diameter using a 16-mm gage length. The HCF tests were performed in air with specimens 3.0 mm in diameter using a 14-mm gage length, an R ratio of 0.1 in the load-control mode, and a frequency of around 80 Hz.

The microstructures and deformation behavior were evaluated using optical microscopy, scanning electron microscopy (SEM), and transmission electron microscopy (TEM). Thin foils for TEM observation were prepared by twin-jet polishing at 233 K with a mixed solution of 10 vol pct H_2SO_4 and 90 vol pct ethanol.

III. RESULTS AND DISCUSSION

A. *Microstructure*

The average size of prior B2 grains was 100 μm after annealing at 1423 K for 3.6 ks and water quenching. Figure 1 shows the microstructures of the Ti-22Al-27Nb alloy cooled from the annealing temperature of 1423 K at four different cooling rates of 0.003 K/s, 0.03 K/s, 0.1 K/s, and water quenching (designated as the 0.003 K/s-cooled, 0.03 K/s-cooled, 0.1 K/s-cooled, and water-quenched specimen, respectively). The lamellar morphology is summarized in Table I. The morphological features of O-phase lamellae, colony size, and lamellae width are seen to be strongly dependent on the cooling rate. The very slow cooling rate of 0.003 K/s resulted in several colonies of similarly aligned O-phase lamellae (gray area) within the prior B2 grains and a nearly continuous α_2 phase (black area) of about 5 μm in width at the grain boundaries[5,7,13] (Figure 1(a)). Although final heat treatment was performed in the (B2 + O) two-phase region, the microstructure maintained the grain boundary α_2 phase, but the rim O phase was observed around the α_2 phase. The size of each colony was determined to be in the range of 100 to 200 μm. The width of the O-phase lamellae was about 4 μm. The B2 phase (bright area) was present as thin films between the O-phase lamellae. The slow cooling rate of 0.03 K/s led to smaller colonies ranging from 30 to 100 μm in size, a narrower grain boundary α_2 phase, and thinner O-phase lamellae of about 2 μm in width (Figure 1(b)). In addition, O-phase lamellae with a type of basketweave morphology were present in the central area of the prior B2 grains. The further refinement of the lamellar morphology could be accomplished at a fast cooling rate of 0.1 K/s (Figure 1(c)). At this cooling rate, most of the area in the prior B2 grains was occupied by the O-phase lamellae with a type of basketweave morphology, and the colonies with limited growth of O-phase lamellae were only seen adjacent to the grain boundaries. Water quenching and the subsequent stabilization annealing at 1123 K for 118.8 ks produced very fine O-phase lamellae with a tweed-like morphology[20] and a thin continuous O phase of about 2 μm in width at the prior B2 grain boundaries (Figure 1(d)). Since the water quenching retained the B2 phase, this microstructural morphology was produced during the subsequent stabilization annealing.

Figure 2(a) shows the TEM micrograph of the 0.003 K/s-cooled specimen. It can be seen that the B2 phase is present between the O-phase lamellae as thin films. The selected area diffraction pattern (SADP) of Figure 2(a) is shown in Figure 2(b), and the diffraction patterns are identified in Figure 2(c). The indexing result of SADP shows that there is a crystallographic relationship between the B2 and O phases: $[111]_{B2}//[110]_o$, $(10\bar{1})_{B2}//(00\bar{1})_o$, or $(01\bar{1})_{B2}//(0\bar{2}\,\bar{1})_o$. This relationship is known as the Burger's relationship. This observation result is in agreement with previous reports by other researchers on orthorhombic alloys.[5,17–20]

Figure 3 shows the high-resolution TEM micrograph of the O/B2 phase interface in the Ti-22Al-27Nb alloy annealed at 1423 K and cooled at the rate of 0.003 K/s. It is clear that the O/B2 phase interface is semicoherent. The lattice lines of the O and B2 phases indicated by the arrow show a crystallographic relationship and a semicoherency between two phases.

Table I. Heat-Treatment Conditions and Lamellar Morphology of Ti-22Al-27Nb

	Heat-Treatment Conditions			Lamellar Morphology		
Specimen Designation	Solution Treatment (Temperature (K)/ Time (ks))	Cooling Rate (K/s)	Annealing Treatment (Temperature (K)/ Time (ks))	Morphological Features of O-Phase Lamellae	Colony Size (μm)	Lamellae Width (μm)
0.003 K/s-cooled	1423/3.6	0.003	1123/118.8/FC	colony (Fig. 1(a))	100 to 200	4
0.03 K/s-cooled	1423/3.6	0.03	1123/118.8/FC	mostly colony (Fig. 1(b))	30 to 100	2
0.1 K/s-cooled	1423/3.6	0.1	1123/118.8/FC	mostly basket-weave (Fig. 1(c))		1
Water quenched	1423/3.6	WQ	1123/118.8/FC	tweed-like (Fig. 1(d))		*

WQ: water quenching (about 130 K/s[16]), FC: furnace cooling, and *: O-phase lamellae with tweedlike morphology are very thin and were difficult to resolve by SEM.

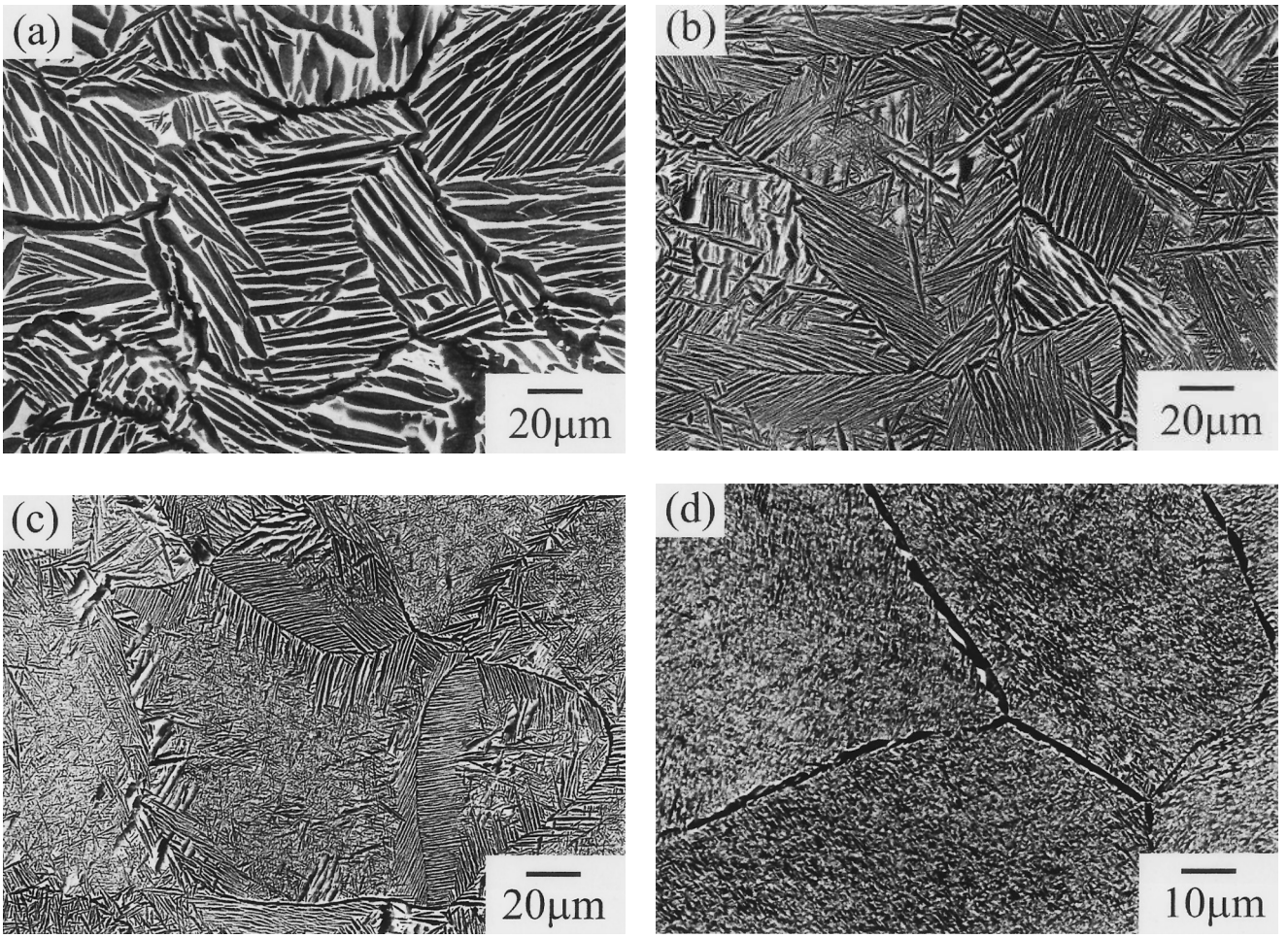

Fig. 1—SEM micrographs of the Ti-22Al-27Nb alloy annealed at 1423 K and cooled at the rates of (*a*) 0.003 K/s, (*b*) 0.03 K/s, (*c*) 0.1 K/s, and (*d*) water quenching.

B. *Tensile Properties*

Table II summarizes the room-temperature tensile properties of the Ti-22Al-27Nb alloy cooled from 1423 K at four different cooling rates. These data are the average of at least two specimens. Increased cooling rates, leading to the refinement of colony size and O-phase lamellae width, increased the yield stress and tensile strength. For example, tensile strength increased from 774 to 976 MPa as the cooling rate increased from 0.003 to 130 K/s (water quenching). Contrary to the tensile strength, increasing the cooling rate decreased ductility. For example, tensile elongation decreased from 11.9 to 7.0 pct as the cooling rate increased from 0.003 to 130 K/s.

Higher-magnification SEM micrographs of tensile-fractured surfaces are shown in Figure 4 for 0.003 K/s-cooled, 0.1 K/s-cooled, and water-quenched specimens. The dependence of fracture path on microstructure is clear from these micrographs. A 0.003 K/s-cooled specimen was broken by the transgranular fracture, and the fracture path was very irregular (Figure 4(a)). This micrograph also shows that there are many elongated microfacets, bounded by tear ridges, on the fracture surface. To reveal the underlying microstructure beneath the fracture surface, a fractured tensile specimen with mutually matching surfaces was sectioned parallel to the tensile axis, as shown in Figure 5. It is seen that the tensile fracture of a 0.003 K/s-cooled specimen was caused by cleavage fracture across the colonies. It is also evident that microfacets and tear ridges seen on the fracture surfaces correspond to the cleavage of individual, similarly aligned O-phase lamellae and the fracture of the thin B2 phase, respectively. These fractographic features are similar to those seen in conventional α-β titanium alloys such as Ti-6A1-4V with a colony microstructure.[21–24] The TEM observation revealed that the planar slip passed through the interface between the O and B2 phases, as shown in Figure 6. Because of this transmission of the slip band, an offset occurred during tensile deformation. The B2 phase was split in two corresponding to the slip line of the O phase, as shown in Figure 6(a). The slip line was composed of many dislocations, as shown in Figure 6(b). Contrary to the 0.003 K/s-cooled specimen, the 0.1 K/s-cooled specimen exhibits a very flat fracture path with traces of cleavage fractures of very fine basketweave O-phase lamellae on the fracture surfaces (Figure 4(b)). A water-quenched specimen exhibits a very irregular fracture path with a mixture of transgranular and intergranular fracture modes (Figure 4(c)). Many grain boundary cracks associated with intergranular fractures are present on the fracture surface.

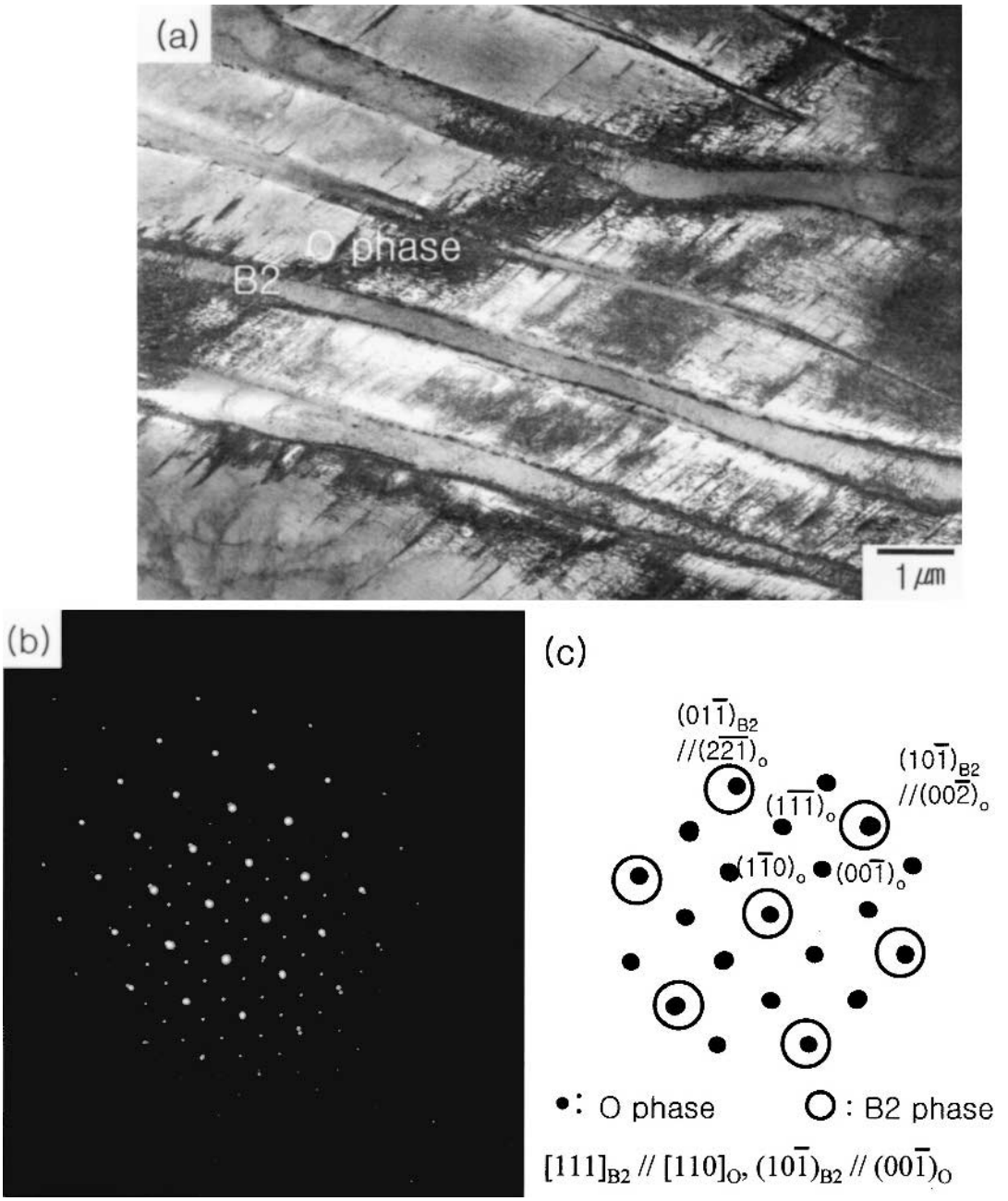

Fig. 2—(*a*) TEM micrograph of the Ti-22Al-27Nb alloy annealed at 1423 K and cooled at the rate of 0.003 K/s. (*b*) SADP taken from (a). (*c*) Indexing result of the SADP.

C. *HCF Properties*

Figure 7 shows the room-temperature HCF curves of the Ti-22Al-27Nb cooled under the four different cooling conditions. It is evident that, as compared to the 0.003 K/s-cooled specimen, the increasing cooling rate increased the HCF strength over the entire cycle range. The HCF strength at 10^7 cycles of 0.003 K/s-cooled, 0.03 K/s-cooled, 0.1 K/s-cooled, and water-quenched specimens was 450, 540, 620, and 680 MPa, respectively. Since the tensile strength of these specimens increased as a result of refining the colony sizes and O-phase lamellae width, part of the fatigue improvement can be attributed to improved strength. To demonstrate that the fatigue improvement was also the result of the improved resistance to fatigue associated with this microstructural refinement, the fatigue ratio of HCF strength to ultimate tensile strength was calculated under the four conditions. If the calculated fatigue ratio is not constant but instead shows a microstructural dependence, a part of the observed fatigue improvement can be attributed to microstructural refinement. Although all the specimens we tested broke before reaching their ultimate tensile strength, we assumed from the tensile curves that the tensile strength is almost equal to the ultimate tensile strength. As shown in Table I, the fatigue ratio at 10^7 cycles of 0.003 K/s-cooled, 0.03 K/s-cooled, 0.1 K/s-cooled, and water-quenched specimens was 0.58, 0.65, 0.67, and 0.70, respectively. We can see that the fatigue ratio is not

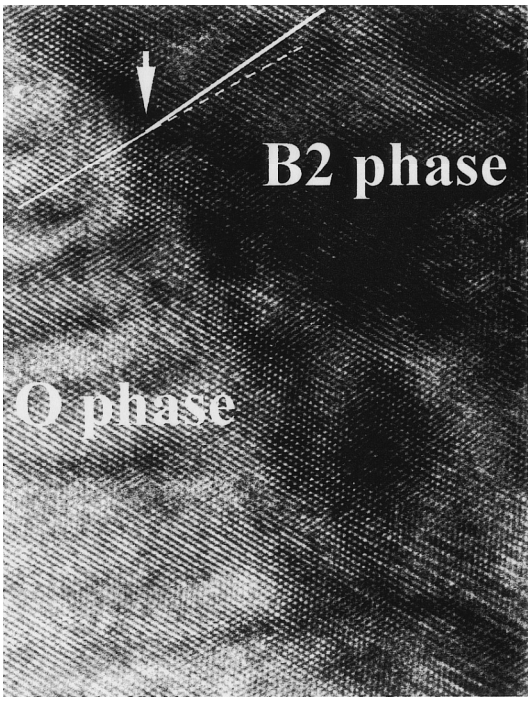

Fig. 3—TEM micrograph of the O/B2-phase interface in the Ti-22Al-27Nb alloy annealed at 1423 K and cooled at the rate of 0.003 K/s, showing that the O/B2 phase interface is semicoherent.

Table II. Tensile and HCF Properties of Ti-22Al-27Nb Alloy with Varying Lamellar Morphology

Specimen Designation	$\sigma_{0.2}$ (MPa)	UTS (MPa)	Tens. EL (Pct)	σ_F (MPa)	S
0.003 K/s-cooled	603	774	11.9	450	0.58
0.03 K/s-cooled	668	835	11.2	540	0.65
0.1 K/s-cooled	715	945	8.3	620	0.66
Water-quenched	814	976	7.0	680	0.70

$\sigma_{0.2}$: yield stress, UTS: ultimate tensile strength, Tens.El.: tensile elongation, σ_F: HCF strength at 10^7 cycles, S: ratio of σ_F to UTS, and WQ: water quenching (about 130 K/s[16]).

constant: instead, it increases with increasing cooling rate. These results clearly confirm that part of fatigue improvement is the result of microstructural refinement.

The SEM examinations of the fatigued specimens are shown in Figures 8, 9, and 10 for the 0.003, 0.03, and 0.1 K/s-cooled specimen, respectively. Most specimens failed due to subsurface crack initiation, and every fatigue initiation site contained a flat facet (Figures 8(a), 9(a), and Figure 10(a)). As shown in these microstructures, the cooling rate dictated the facet size, which was the largest (about 200 μm in diameter) in the 0.003 K/s-cooled specimen (Figure 8(a)) and the smallest (about 80 μm in length and 50 μm in width) in the 0.1 K/s-cooled specimen (Figure 10(a)). It has been generally recognized in titanium alloys that most of the HCF life is spent in the fatigue initiation stage.[21] Therefore, it seems reasonable to argue that fatigue life is closely dependent on facet size.

To correlate the facet size with the microstructure and, as a result, to gain an understanding of the fatigue initiation mechanism, the initiation facet and the underlying microstructure were concurrently observed using a precision sectioning

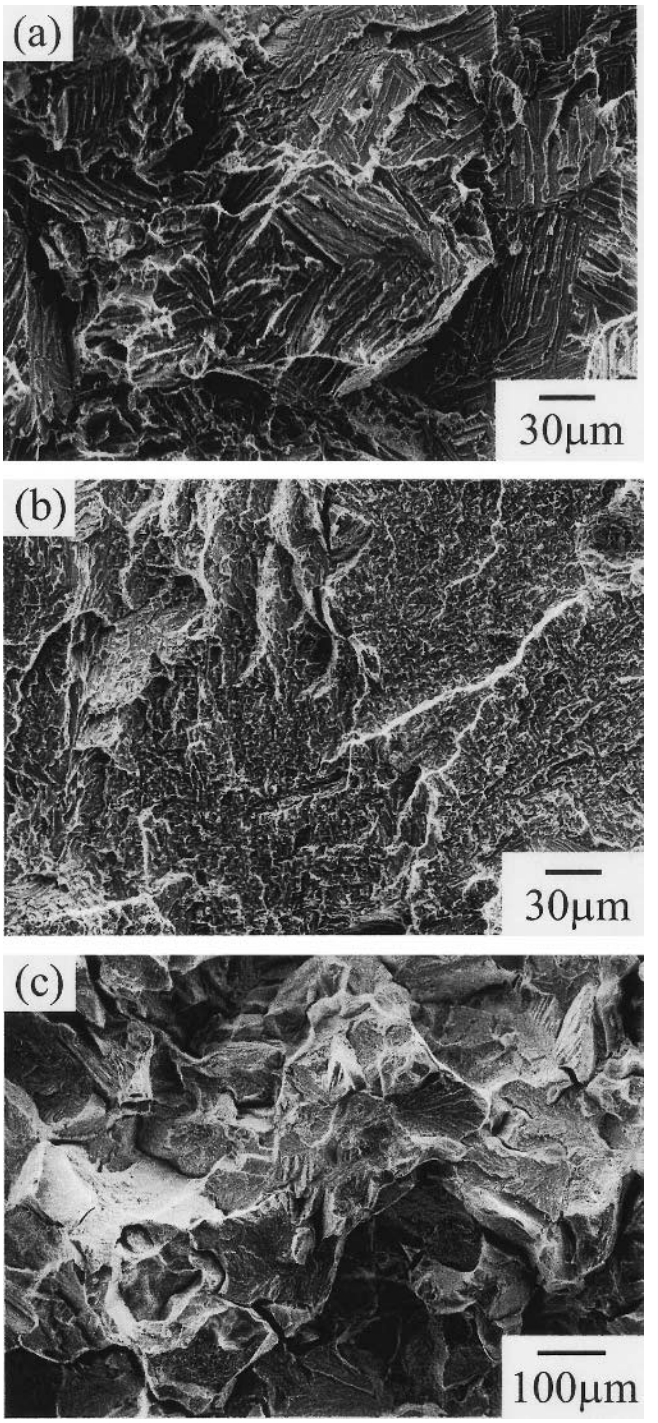

Fig. 4—Tensile fractured surfaces of the Ti-22Al-27Nb alloy annealed at 1423 K and cooled at the rates of (*a*) 0.003 K/s, (*b*) 0.1 K/s, and (*c*) water quenching.

method.[22,23] In this method, the fatigued specimen was sectioned perpendicular to the fracture surface through the section line. After polishing and etching the sectioned surface, the mounting material was resolved, enabling concurrent observation of the initiation facets and the underlying microstructure. Figure 8(b) shows the concurrent observation of the initiation facet and the underlying microstructure for the 0.003 K/s-cooled specimen. As seen from the underlying microstructure, the fatigue crack initiated within one colony, which indicates that

Fig. 5—Microstructure beneath the tensile fractured surfaces of the Ti-22Al-27Nb alloy with surfaces matched to each other. This alloy was annealed at 1423 K and cooled at the rate of 0.003 K/s.

the size of the initiation facet corresponds to that of one colony and that the one colony of similarly aligned O-phase lamellae can be regarded as a single grain. As is the case in the tensile fracture surfaces (Figure 4(a)), the initiation facet consists of many elongated microfacets, each of which is bounded by tear ridges. It is also clear that these microfacets and tear ridges correspond to the fracture of individual, similarly aligned O-phase lamellae and the thin B2 phase, respectively. The initiation facet and the underlying microstructure for the 0.03 K/s-cooled specimen are shown in Figures 9(b) and (c). In Figure 9(b), the tensile axis is perpendicular to the photograph. Two large facets are seen at the fatigue initiation site. This type of fatigue initiation is reported to occur as a multifacet initiation in conventional α-β titanium alloys with a colony microstructure.[22] The size of each initiation facet was about 100 μm, equivalent to that of one colony within prior B2 grains in this specimen. The underlying microstructure (Figure 9(b)) shows that each of two facets is inclined at 45 deg to the tensile axis, which is a favorable angle for shear-related crack initiation, since it coincides with maximum shear direction. Therefore, it can be concluded that the fatigue crack initiated in a shear mode across the colony in both the 0.003 and 0.03 K/s-cooled specimens. Figure 9(c) and the inset show a higher magnification of the underlying microstructure. We can see that there is an intense slip band (indicated by the arrow), located just beneath the initiation facet and parallel to the facet plane. It is also seen

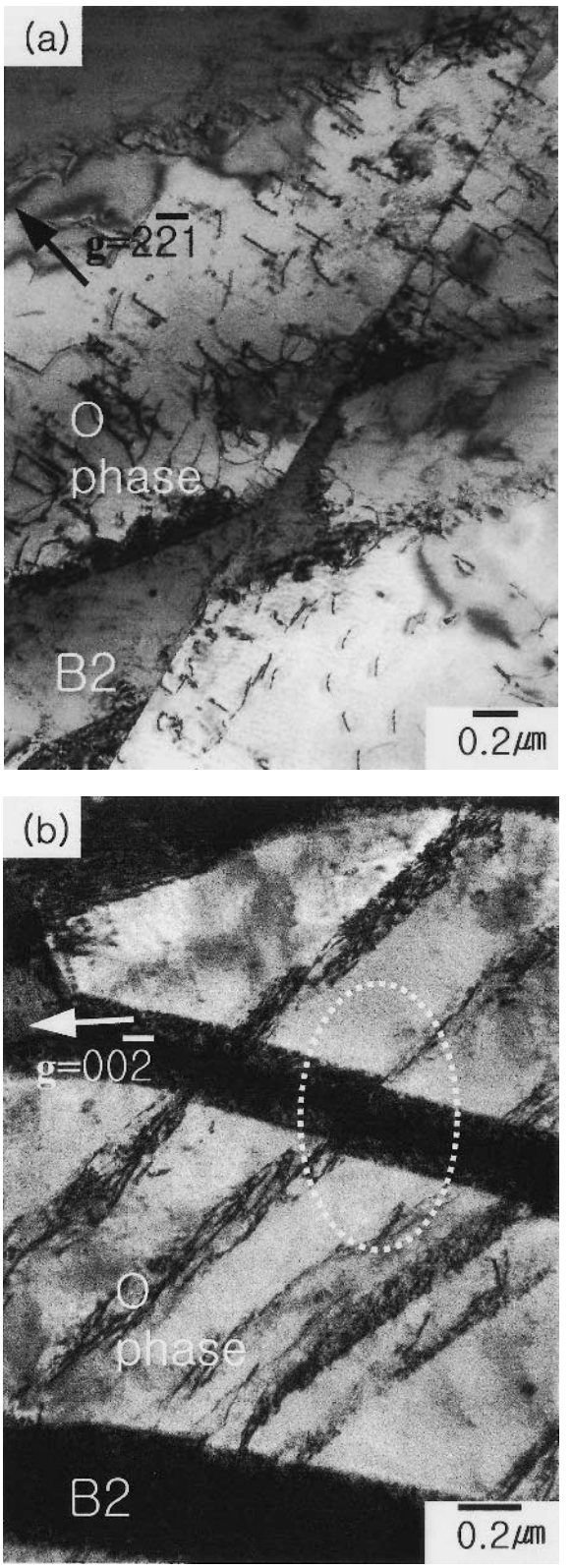

Fig. 6—TEM observation of tensile fractured Ti-22Al-27Nb alloy. (*a*) Planar slip passing through the O/B2 interface and (*b*) offset of B2 phase (indicated by circle) and slip line composed of numerous dislocations. This alloy was annealed at 1423 K and cooled at the rate of 0.003 K/s.

that there exists an offset of the colony microstructure across this intense slip band. The presence of this intense slip band

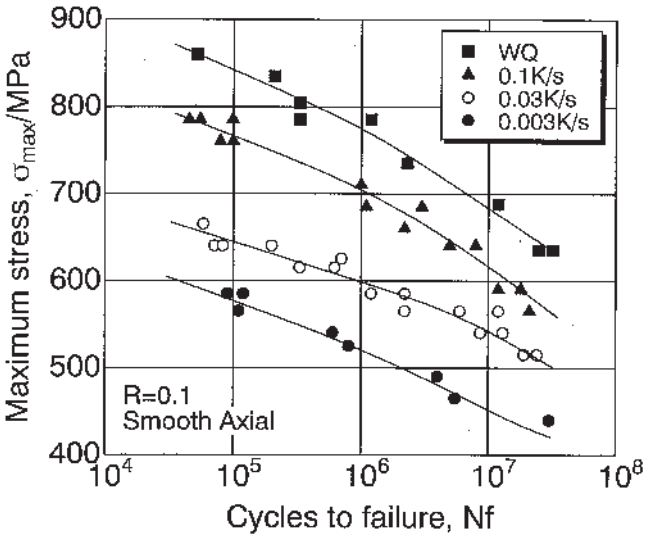

Fig. 7—Room-temperature HCF curves of the Ti-22Al-27Nb alloy, which was annealed at 1423 K and cooled at the rates of 0.003 K/s, 0.03 K/s, 0.1 K/s, and water quenching.

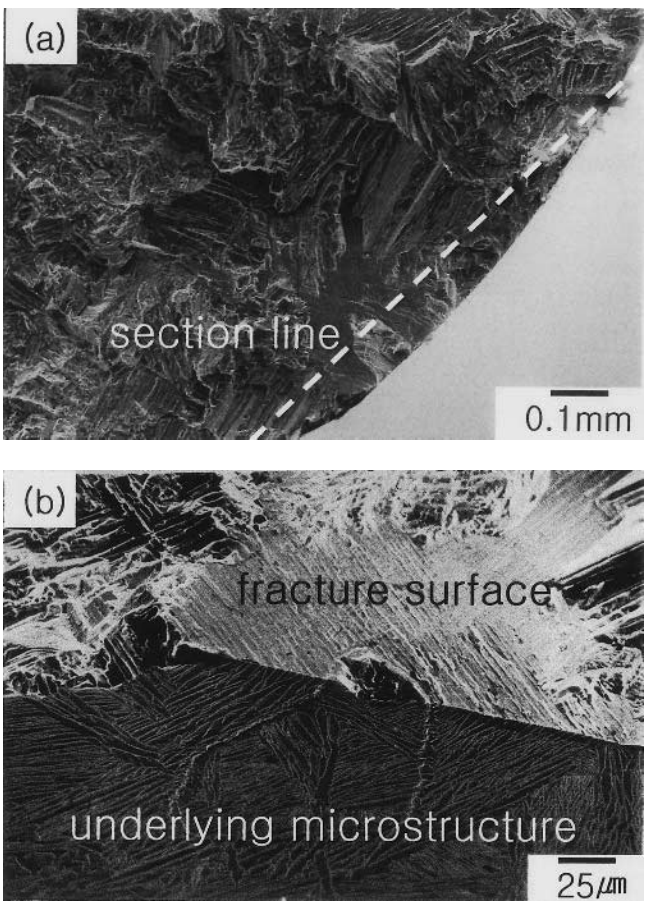

Fig. 8—Fatigue crack initiation of the Ti-22Al-27Nb alloy annealed at 1423 K and cooled at the rate of 0.003 K/s. (*a*) General view of fatigue crack initiation site and (*b*) concurrent observation of the fatigue initiation facet and the underlying microstructure.

strongly suggests that the shear fracture for the fatigue initiation was caused by the slippage of the intense slip band. The initiation facet and the underlying microstructure for the 0.1 K/s-cooled specimen are shown in Figure 10(b). It is clear that that the fatigue crack initiated within the colony microstructure located adjacent to the grain boundary.

As described previously, the fatigue crack initiated in a shear mode within the colony irrespective of the cooling rate and, accordingly, irrespective of the initiation facet size. These observations mean that the slip path corresponded to that of one colony of similarly aligned O phase lamellae.

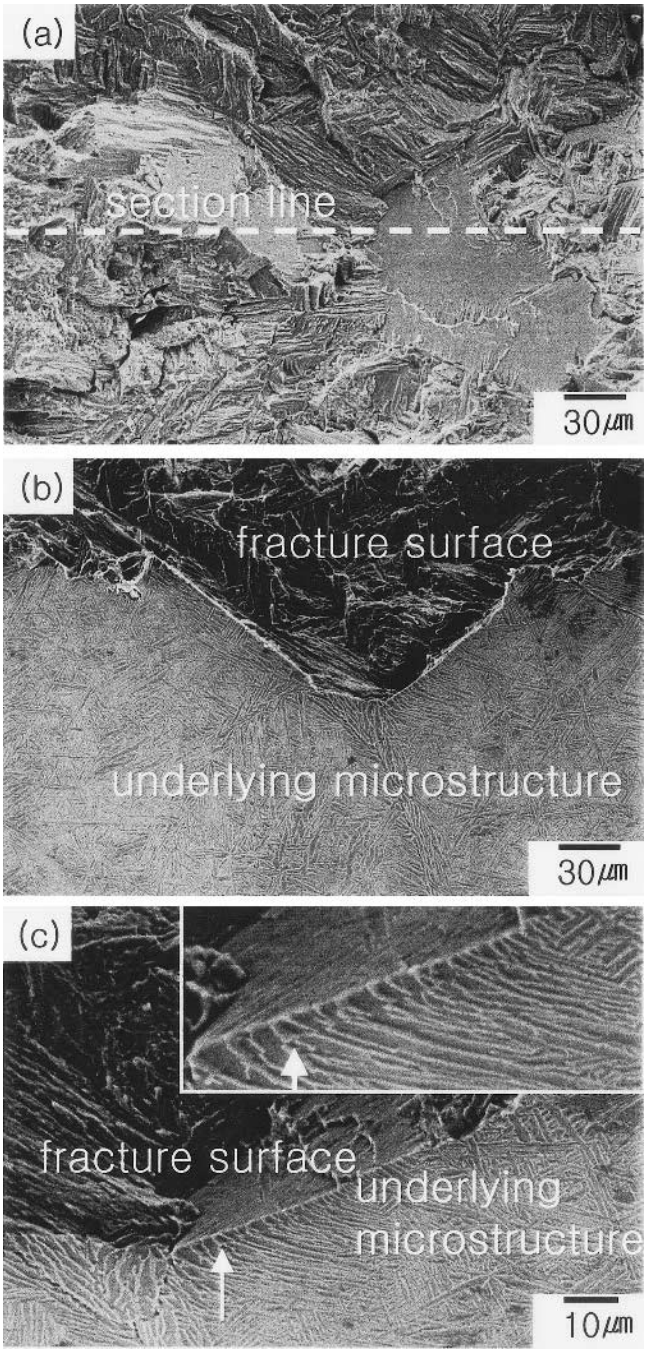

Fig. 9—Fatigue crack initiation of the Ti-22Al-27Nb alloy annealed at 1423 K and cooled at the rate of 0.03 K/s. (*a*) General view of fatigue crack initiation site, (*b*) concurrent observation of the fatigue initiation facet and the underlying microstructure, and (*c*) higher magnification view of the underlying microstructure showing the existence of an intense slip band (indicated by arrow) beneath the initiation facet.

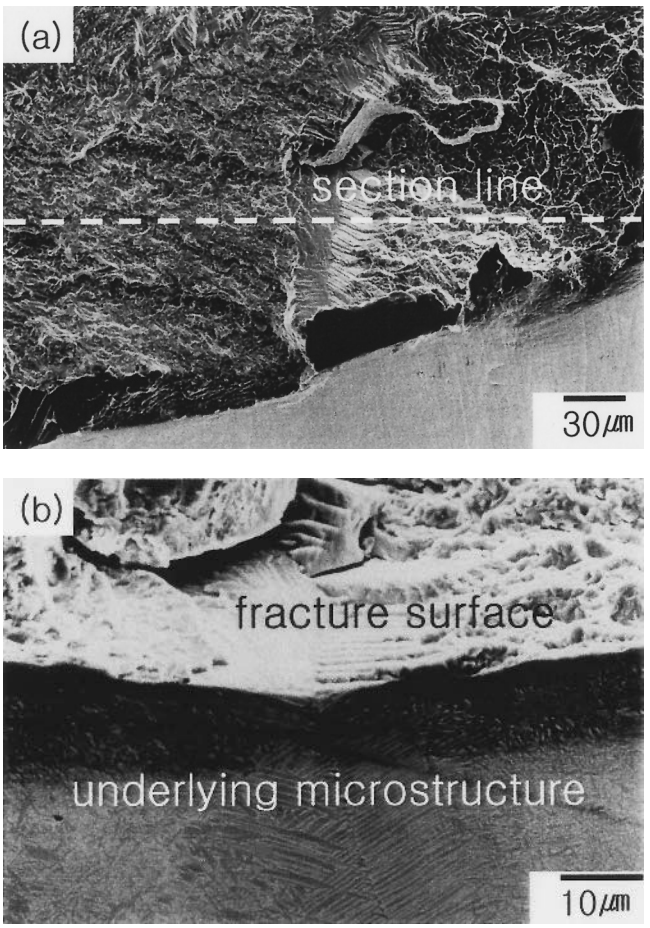

Fig. 10—Fatigue crack initiation of the Ti-22Al-27Nb alloy annealed at 1423 K and cooled at the rate of 0.1 K/s. (*a*) General view of fatigue crack initiation site and (*b*) concurrent observation of the fatigue initiation facet and the underlying microstructure.

Therefore, colony size is likely a major controlling factor in determining the fatigue improvement due to the microstructural refinement of the lamellar morphology. The lowest fatigue life of the 0.003 K/s-cooled specimen, with a large colony size, can be explained by the long slip path associated with this microstructure, since the long slip path can easily cause slippage of the intense slip bands and high stress concentrations at the colony.[22,24] Thus, the HCF strength increased when this microstructural parameter decreased.

As described previously, the O-phase lamellae width decreased with increasing cooling rate. Therefore, the lamellae width as well as the colony size may be the controlling microstructural factors in influencing the HCF strength.[25,26] It may be reasonable to consider that the narrower lamellaer size and consequent dense O/B2 phase interfaces can be much more helpful to improve the resistance to fatigue crack initiation by the restriction of the dislocation movement in the O-phase lamellae and also the retardation of slip transmission through O/B2-phase interfaces. However, the extent to which the lamellae width exerts improvement of the HCF strength requires further consideration.

As shown in Figure 11, the appearance of the initiation facet of the water-quenched specimen was quite different than those of the other three specimens. The fatigue initiation facet showed a featureless appearance. Judging from this appearance and also from the fact that there existed many grain boundary cracks on the tensile fractured surface (Figure 4(c)), the fatigue initiation appears to be associated with a shear cracking along the boundary between the continuous grain boundary O phase and the adjacent prior B2 grain. The present observations strongly indicate that fatigue initiation could occur much more easily at the grain boundary than in the interior of the grain. The reason for this entirely different fatigue initiation mechanism in the water-quenched specimen can be attributed to the increased difficulty of the slip band formation and subsequent slip-off of the slip band in the O-phase lamellae. As shown in Figure 1(d), the O-phase lamella in the water-quenched specimen was very fine, and therefore, it seemed that the dislocation movement across the O-phase lamellae was not so prevalent during the fatigue test compared to the other three conditions. This less active dislocation movement could lead to the suppression of slip band formation and subsequent slip-off of the slip band. Due to such difficulties associated with the slip-off of the slip band, the water-quenched specimen was believed to have the highest HCF strength and fatigue ratio. Finally, the fatigue initiation occurred in the other possible fatigue initiation sites, *i.e.*, at the grain boundary, which can be regarded as the easiest fatigue initiation site for the microstructure associated with the water-quenched specimen.

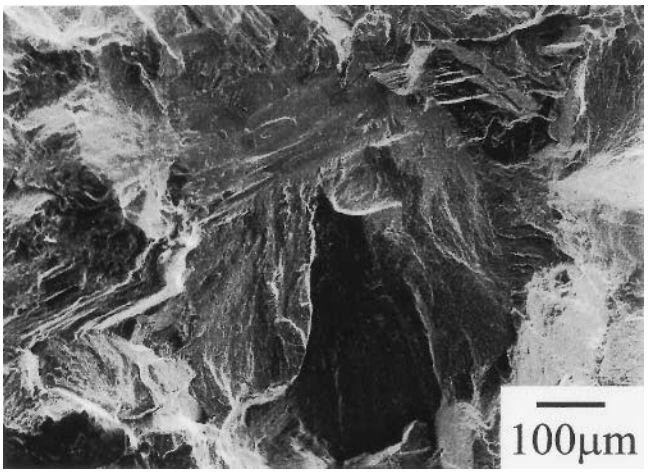

Fig. 11—Fatigue crack initiation of the Ti-22Al-27Nb alloy annealed at 1423 K and water quenched.

One of the authors has previously evaluated the HCF strength and fatigue ratio of various near-α type and α-β type titanium alloys with lamellar microstructures. These alloys included Ti-6Al-2Sn-4Zr-2Mo, Ti-6Al-4V, Ti-6Al-2.7 Sn-4Zr-0.4Mo-0.45Si, Ti-6Al-1.7Fe-0.1Si, and Ti-5Al-2.5Fe and were produced by the conventional blended elemental powder metallurgy method using extra-low chlorine titanium powder.[27,28] Fatigue tests on these alloys were conducted under the same test conditions and the same fatigue test machine as the present specimens. The HCF strength and fatigue ratios at 10^7 cycles of these alloys were 412, 412, 420, 350, and 441 MPa, and 0.42, 0.45, 0.43, 0.33, and 0.45, respectively. By comparing these values with the present results, we can see that, even under the conditions of the coarsest lamellar morphology, a Ti-22Al-27Nb alloy exhibits considerably higher HCF strength and fatigue ratio. Since the fatigue initiation period dominates most of fatigue life,

this superior HCF performance may suggest that the resistance to fatigue initiation is much higher in a Ti-22Al-27Nb alloy than in conventional titanium alloys.

To analyze the Burger's vector of dislocations in the O phase of the present Ti-22Al-27Nb alloy with lamellar microstructure, the TEM observation technique known as the "$\mathbf{g}\cdot\mathbf{b} = 0$ invisibility criterion" was used. Figure 12 shows TEM microstructures of the 0.003 K/s-cooled specimen fatigue tested at a maximum stress of 539 MPa. Typical cell structures that are usually observed in fatigue-tested specimens were not observed. This is due to the narrow O-phase lamella microstructure. Dislocations in the O phase after

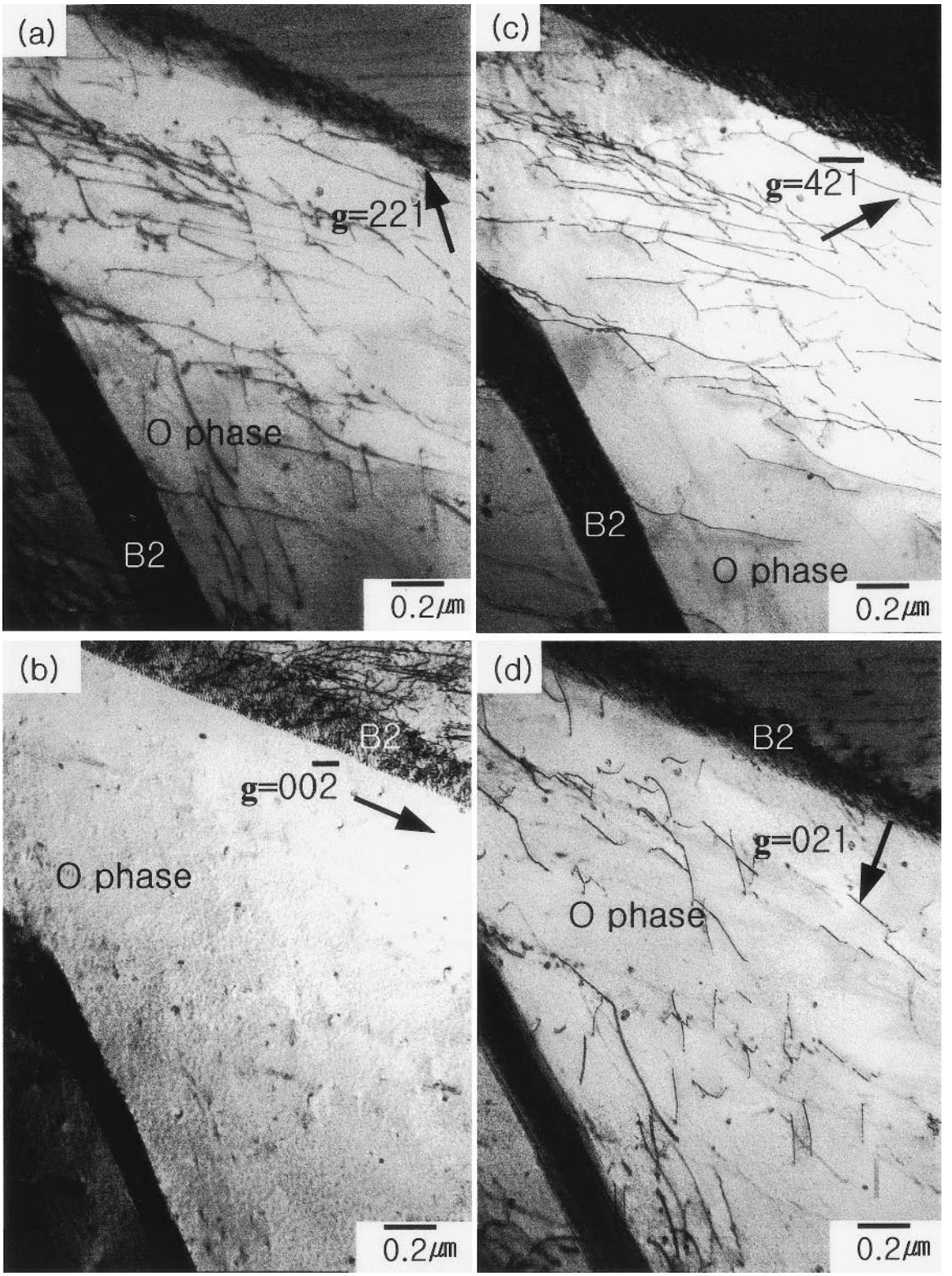

Fig. 12—Dislocations in the fatigued Ti-22Al-27Nb alloy annealed at 1423 K and cooled at 0.03 K/s: (*a*) $\mathbf{g} = [221]$, (*b*) $\mathbf{g} = [002]$, (*c*) $\mathbf{g} = [421]$, and (*d*) $\mathbf{g} = [021]$.

fatigue testing were analyzed under various diffraction conditions. The diffraction vector of $\mathbf{g} = [221]$ in Figure 12(a) is the visible condition of all slip systems in the Ti_2AlNb orthorhombic crystal system. On the other hand, all dislocations are invisible in Figure 12(b), where $\mathbf{g} = [002]$. This diffraction vector, $\mathbf{g} = [002]$, is the vector that distinguishes prismatic dislocations from other slip systems. Only prismatic dislocations should be visible under these conditions. Therefore, the dislocations shown in Figure 12 may not be on the prismatic plane. The dislocations in Figure 12(a) can be classified into two groups, as shown in Figures 12(c) and 12(d) with different diffraction conditions. The dislocations observed at $\mathbf{g} = [4\bar{2}\bar{1}]$(Figure 12(c)) are invisible under the diffraction condition of $\mathbf{g} = [021]$ (Figure 12(d)), which is a typical condition for determining the basal slip system, $\mathbf{b} = 1/2[100](001)$. The dislocations on the basal plane are invisible under the diffraction condition of $\mathbf{g} = [0\bar{2}1]$. However, a pyramidal slip system of $\mathbf{b} = 1/2[1\bar{2}0](2\bar{1}2)$ is visible under the diffraction condition of $\mathbf{g} = [4\bar{2}\bar{1}]$ and visible under the diffraction condition of $\mathbf{g} = [021]$. Therefore, the dislocations shown in Figures 12(c) and 12(d) can be determined to be basal and pyramidal dislocations, respectively. However, further work is needed to correlate these dislocation characteristics with the HCF mechanism.

IV. CONCLUSIONS

An orthorhombic Ti-22Al-27Nb alloy with varying lamellar morphologies was produced and evaluated in terms of its microstructure, and tensile and HCF behavior.

1. The lamellar morphology was strongly dependent on the cooling rate from the annealing temperature. A slower cooling rate of 0.003 K/s, for example, resulted in several large packets or colonies of similarly aligned O-phase lamellae and a nearly continuous massive α_2 phase at the prior B2 grain boundaries, while a faster cooling rate of 0.1 K/s led to the refinement of colony size and the O-phase lamellae width. Water quenching produced a very fine tweed-like microstructure with a thin continuous O phase at the prior B2 grain boundaries.
2. The refinement of lamellar morphology, *i.e.*, reducing the colony size and the O-phase lamellae width, increased the yield stress, tensile strength, and HCF strength. Since the ratio of HCF strength to tensile strength also increased, a part of the increase in HCF strength was thought to be due to this microstructural refinement.
3. The concurrent observation of the initiation facet and the underlying microstructure revealed that fatigue cracks initiated in shear mode within the colony and the initiation facet size, namely, slip path, corresponded to that of one colony. Therefore, the colony size is likely a major controlling factor in determning fatigue improvement due to the microstructural refinement of lamellar morphology. Additionally, the narrow width of the O and B2 phases was thought to be helpful to enhance the HCF strength by the restriction of the dislocation movement in the O-phase lamellae and also the retardation of slip transmission through O/B2 phase interfaces. In the water-quenched specimen, the fatigue crack initiation appeared to be associated with shear cracking along the boundary between the continuous grain-boundary O phase and the prior B2 grain.

ACKNOWLEDGMENTS

This research was performed under the Japan–Korea bilateral cooperative research program. The authors gratefully acknowledge the financial support of both the Japanese and Korean governments.

REFERENCES

1. D.A. Koss, D. Banerjee, D.A. Lukasak, and A.K. Gogia: *High Temperature Aluminides and Intermetallics*, TMS, Warrendale, PA, 1990, pp. 175-96.
2. Y.-W. Kim: *J. Met*., 1989, vol. 41, pp. 24-30.
3. R.G. Rowe: *Microstructure/Property Relationship in Titanium Aluminides and Alloys*, TMS, Warrendale, PA, 1991, pp. 387-98.
4. R.G. Rowe: *Titanium '92—Science and Technology*, TMS, Warrendale, PA, 1993, pp. 343-50.
5. C.J. Boehlert, B.S. Majumdar, V. Seetharaman, and D.B. Miracle: *Metall. Mater. Trans. A*, 1999, vol. 30A, pp. 2305-23.
6. C.J. Boehlert and D.B. Miracle: *Metall. Mater. Trans. A*, 1999, vol. 30A, pp. 2349-67.
7. J.W. Zhang, C.S. Lee, D.X. Zou, S.Q. Li, and J.K.L. Lai: *Metall. Mater. Trans. A*, 1998, vol. 29A, pp. 559-64.
8. Y. Mao, S.L. Li, J.W. Zhang, J.H. Peng, D.X. Zou, and Z.Y. Zhong: *Intermetallics*, 2000, vol. 8, pp. 659-62.
9. J. Kumpfert and C. Leyens: *Structural Intermetallics 1997*, TMS, Warrendale, PA, 1997, pp. 895-04.
10. J. Kumpfert and W.A. Kaysser: *Z. Metallkd*., 2001, vol. 92, pp. 128-33.
11. A.K. Gogia, T.K. Nandy, D. Banerjee, T. Carisey, J.L. Strudel, and J.M. Franchet: *Intermetallics*, 1998, vol. 6, pp. 741-48.
12. F. Tang and M. Hagiwara: *Metall. Mater. Trans. A*, 2003, vol. 34A, pp. 633-43.
13. S. Emura, A. Araoka, and M. Hagiwara: *Scripta Mater*., 2003, vol. 48, pp. 629-34.
14. S.J. Yang, S.W. Nam, and M. Hagiwara: *J. Alloys Compounds*, 2003, vol. 350, pp. 280-87.
15. J.H. Peng, Y. Mao, S.Q. Li, and X.F. Sun: *Mater. Sci. Eng*., 2001, vol. A299, pp. 75-80.
16. G. Lutjering, J. Albrecht, and O.M. Ivasishin: *TITANIUM '95*, The Institute of Materials, London, 1995, pp. 1187-94.
17. L.A. Bendersky, W.G. Bottinger, and A. Roytburt: *Acta Metall. Mater*., 1991, vol. 39, pp. 1959-69.
18. F.A. Sadi and C. Servant: *Mater. Sci. Eng*., 2001, vol. A346, pp. 19-28.
19. J.W. Zhang, S.Q. Li, D.X. Zou, W.Q. Ma, and Z.Y. Zhong: *Intermetallics*, 2000, vol. 8, pp. 699-02.
20. K. Ito, L.T. Zhang, V.K. Vasudevan, and M. Yamaguchi: *Acta Mater*, 2001, vol. 49, pp. 963-72.
21. D. Eylon and C.M. Pierce: *Metall. Trans. A*, 1976, vol. 7A, pp. 111-21.
22. D. Eylon: *J. Mater. Sci*., 1979, vol. 14, pp. 1914-22.
23. D. Eylon and J.A. Hall: *Metal. Trans. A*, 1977, vol. 8A, pp. 981-90.
24. J.C. Williams and G. Luetjering: *TITANIUM '80, Science and Technology*, The Japan Institute of Metals, Sendai, 1980, pp. 671-81.
25. K.S. Ravichandran, E.S. Dwarakadasa, and D. Banerjee: *Scripta Metall. Mater*., 1991, vol. 25, pp. 2115-20.
26. K.S. Ravichandran: *Acta Metall. Mater*., 1991, vol. 39 (3), pp. 401-10.
27. M. Hagiwara, Y. Kaieda, Y. Kawabe, and S. Miura: *Iron Steel Inst. Jpn. Int*., 1991, vol. 31, pp. 922-30.
28. M. Hagiwara, S.J. Kim, and S. Emura: *Scripta Mater*., 1998, vol. 39 (9), pp. 1185-90.